



Universiteit
Leiden
The Netherlands

Programmable mechanical metamaterials

Florijn, H.C.B.

Citation

Florijn, H. C. B. (2016, November 29). *Programmable mechanical metamaterials*. *Casimir PhD Series*. Retrieved from <https://hdl.handle.net/1887/44475>

Version: Not Applicable (or Unknown)

License: [Licence agreement concerning inclusion of doctoral thesis in the Institutional Repository of the University of Leiden](#)

Downloaded from: <https://hdl.handle.net/1887/44475>

Note: To cite this publication please use the final published version (if applicable).

Cover Page



Universiteit Leiden



The handle <http://hdl.handle.net/1887/44437> holds various files of this Leiden University dissertation

Author: Florijn, H.C.B.

Title: Programmable mechanical metamaterials

Issue Date: 2016-11-29

A PROGRAMMABLE MECHANICAL METAMATERIAL

In this chapter, based on B. Florijn, C. Coulais, and M. van Hecke, *Programmable Mechanical Metamaterials*, *Physical Review Letters* **113**, 175503 (2014), we create mechanical metamaterials whose response to uniaxial compression can be programmed by lateral confinement, allowing monotonic, non-monotonic and hysteretic behavior. These functionalities arise from a broken rotational symmetry which causes highly nonlinear coupling of deformations along the two primary axes of these metamaterials. First we describe the fabrication process of the metamaterials and the experimental setup used. Then we present the response to uniaxial loading the confined biholar samples. We show that the phenomenology as observed is robust and is also present in numerical simulations. Finally, we introduce a soft mechanism model which captures the programmable mechanics, and outline a general design strategy for confined mechanical metamaterials.

2.1 Introduction

We start by briefly revising the monoholar sheet [42, 44–47], a quasi-2D elastic slab of material patterned by a regular array of holes (Fig. 2.1(a)). The arrow in Fig. 2.1(a) indicates a 90° rotation symmetry, one of the symmetries associated with this hole pattern, when rotating around the blue dot in the center. A biholar sheet, Fig. 2.1(b), a quasi-2D elastic slab of material patterned by a regular array of *large and small holes*, breaks this 90° rotation symmetries. When rotating this pattern around the blue dot it only exhibits 180° rotational symmetries.

When uniaxially compressing a monoholar sheet sufficiently far, a pattern transformation occurs (Fig. 1.6(a)-(b)). This pattern is independent of the direction of compression: whether a given hole will become an ellipse with its main axis orientated in the x - or y -direction, does not depend on the direction of compression. Rather this orientation is set by imperfections of the sheet, and for a perfect sheet, the pattern transformation is a form of spontaneous symmetry breaking induced by buckling [42, 44–47].

Compressing a biholar patterned sheet will also result in a pattern transformation, from spherical holes to orthogonal ellipses. However, the orientation of the ellipses in the compressed state, now depends on the direction of compression, (Fig. 2.2(a)-(c)). By breaking the 90° rotation symmetry of the original hole pattern, the transformation to ellipses is now no longer a spontaneous symmetry breaking, but rather proceeds smoothly from the circular biholar pattern.

When we compress the biholar sheet in the x -direction, we observe an pattern of large and small ellipses. The major axes of the larger ellipses are orthogonal to the direction of compression. From now we will refer to this pattern as x -polarized, Fig. 2.2b. Likewise, if we compress the biholar sheet in the y -direction the major axis of the larger ellipse is in the x -direction and we will refer to this orientation of the pattern as y -polarized.

The core idea to obtain mechanical metamaterials with tunable mechanical response is illustrated in Fig. 2.2(d). When compressing in both direc-

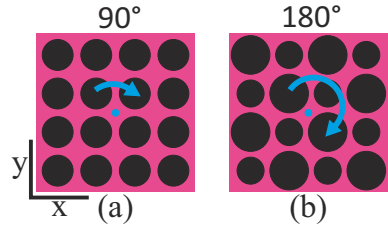


FIGURE 2.1: The difference in hole sizes breaks one of the 90° rotation symmetries present for equal hole sizes.

tions there is a competition between the x and y -polarized pattern, which leads to nontrivial mechanics. We use quasi 2D elastic sheets of thickness 35 μm to avoid out-of-plane buckling. Their 2D structure is shown in Fig. 2.3, with D_1 and D_2 the diameter of the holes and p the pitch, the distance between centers of the holes. We will use the confinement in the x -direction in order to tune the relation between the force and the compression in the y -direction. As we will see in Section 2.4, compressing this confined metamaterial in the y -direction, the material undergoes a pattern switch from a x -polarized to a y -polarized state, as illustrated in Fig. 2.3. Depending on the magnitude of the x -confinement, this pattern switch can be either smooth or discontinuous, and the force displacement curves for the y -deformations can be tuned from monotonic to non-monotonic (unstable) to hysteretic — all for a single biholar sheet. We observe this tunability in experiments on systems of various sizes as well as in numerical simulations of the unit cell — this is a robust phenomenon, Section 2.5. We introduce a simple model that qualitatively captures all these different mechanical behaviors, and which allows a precise study of the bifurcation scenario that underlies this phenomenology, Section 2.6. Finally, we show that the sensitive nature of the hysteretic switching between x and y -polarized patterns can be explored in larger systems, where controlled inhomogeneities lead to multi-stability and giant hysteresis. We suggest that confinement is a general mechanism for a much larger class of programmable mechanical metamaterials, and outline how our model opens a pathway towards rational design of these materials.

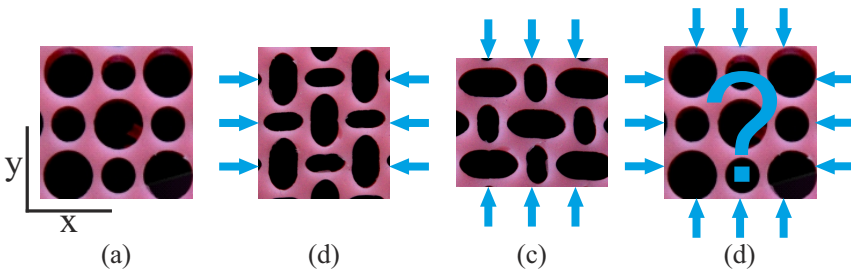


FIGURE 2.2: (a) Detail of an uncompressed biholar sheet. (b) Compressing the sheet in the x -direction (a), results in a pattern with larger and smaller ellipses. The major axis of the larger ellipse is orthogonal to the direction of compression. From now on we will refer to this pattern as x -polarized. (c) Compressing the sheet in the y -direction will result in a y -polarization of the pattern. (d) What will happen if we compress the system in both directions?

2.2. SAMPLES

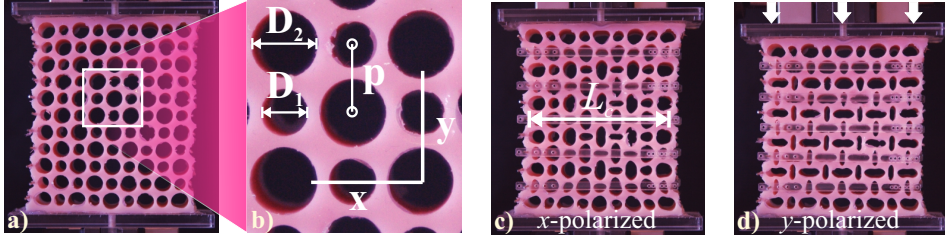


FIGURE 2.3: (a-b) A bi-holar sheet characterized by hole diameters $D_1 = 10$ mm, $D_2 = 7$ mm and pitch $p = 10$ mm. (c) Uniform confinement L_c in the x -direction (by semi-transparent clamps) leads to an x -polarization of the material. (d) Sufficient y -compression of this x -confined material leads to a switch of the polarization, and concomitant non-trivial mechanical behavior. Without x -confinement the pattern will look very similar.

2.2 Samples

We now discuss the fabrication process of the metamaterial. To create these bi-holar sheets, we pour a two components silicone elastomer (Zhermack Elite Double 8, Young's Modulus $E \simeq 220$ kPa, Poisson's ratio $\nu \simeq 0.5$) in a mold which consists of brass cylinders of diameter D_1 and D_2 , precisely placed in the square grid of two laser-cut sidewalls, see Section 2.2.1 and Section 2.2.2, with $p = 10$ mm. We cut the sheets lateral sides and glue their flat bottom and top to Plexiglas plates (Section 2.2.3).

To impose confinement, we glue copper rods of diameter 1.2 mm on the sides of our material, see Fig. 2.8, and use laser cut plastic clamps which have holes at distance L_c to exert a confining strain in the x -direction. determine the polarization of the holes.

In Sections 2.2.1 - 2.2.3 we describe the fabrication process of the holey sheets in detail. In Section 2.2.1 we describe the different molds used to fabricate the different sizes of sheets, followed by a detailed description of the molding process itself in Section 2.2.2. In Section 2.2.3 we describe the last steps we need to perform to prepare the network for experiments, followed by a section about the mechanical properties of the material used to make the holey sheets (Section 2.2.4).

2.2.1 Molds

We created a tunable mold, which allows us to vary D_1 and D_2 and created systems up to 9×11 holes. All quasi-2D sheets have a thickness of 35 mm to avoid out-of-plane buckling. We first describe the mold used for the large holey sheets, followed by the description of the mold used to fabricate the smaller 5×5 sheets.

Large Sheets

We first focus on the creation of samples of maximal size (9×11 holes). These are created by pouring a two component silicone elastomer into a mold. Depicted in Fig. 2.4(a) are the parts that, when assembled, make the mold. Shown are five aluminum parts; three corner parts and two L-shaped parts to make a funnel at the top of the mold to be able to pour the liquid silicone into the assembled mold. Furthermore we use four Acrylic laser cut plates (dimensions $5 \times 35 \times 120$ mm) with four threaded holes in each of them to make the sides of the mold. Also shown are a back and front plate (dimensions $5 \times 140 \times 140$ mm). The back- and front plates contain holes with a diameter of 3 mm in a square lattice with pitch $p = 10$ mm. The metal cylinders are inserted into the back plate to create the hole pattern. Finally we have two acrylic triangular plates. These triangular plates are used to construct a funnel. A spacer is positioned between these triangular plates to separate the funnel into two parts. One of these compartments is used to pour the material. The other compartment is used as a channel for the air to escape when pouring the liquid elastomer in the mold. The mold is assembled using $M6$ screws and butterfly nuts.

To assemble the mold we first connect the three metal corner parts with the four acrylic side plates using twelve $M6$ screws, Fig. 2.4 (b). Note that the bottom metal corner part has two screws threaded into the bottom to, later, position the mold vertically onto a bottom plate. Next we attach the two L-shaped metal corner parts to the top of the mold, together with the two triangular acrylic plates (front and back) and the spacer, to make the funnel. In Fig. 2.4(c) we show how the metal cylinders are inserted into the mold and finally we mount the front plate, Fig. 2.4 (d).

All cylinders have the same height of 5 cm. Their diameter varies from 6 mm to 10 mm. Shown in Fig. 2.4 (e) are three different cylinders, from left to right, with diameter 10, 7 and 7 mm, respectively. Notice the end

2.2. SAMPLES

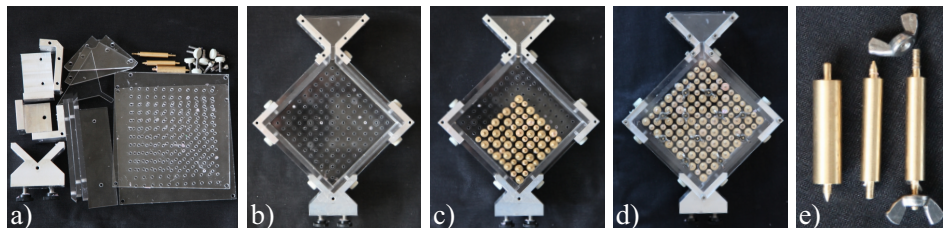


FIGURE 2.4: The assembly of the mold. (a) The mold consists of five metal parts (three corner parts and two L-shaped parts), acrylic top and bottom plates with holes to insert the metal cylinders, four corner plates, metal cylinders and two triangular acrylic plates and an acrylic spacer to make a funnel. (b) The three metal corner parts, four acrylic side plates and the acrylic back plate are mounted together using *M6* screws. Also, the two triangular acrylic plates are attached to the mold with the spacer to make the funnel. (c) The metal cylinders are threaded into the back plate to facilitate the holey pattern. (d) The front plate is mounted onto the mold using *M6* screws and butterfly nuts. (e) Metal cylinders of different sizes and different types.

parts. The left and center cylinder have two milled pins with a length of 4 mm and a diameter of 3 mm. The bottom pin is blunt while the top pin is sharp. This sharp tip makes it easier to attach the top plate onto the mold as the top of the cylinders are 'guided' in to the holes of this plate. The right cylinder has two threaded pins with a lengths of 6 mm and diameter 3 mm to be able to screw a butterfly nut to tighten the back and front plate also in the interior part of the mold. We mount the mold onto a plate with three screws to be able to tilt the mold slightly, which helps to remove the air through the front of the funnel in the mold while pouring silicone in the back.

Small Sheets

For the fabrication of smaller samples we use the the same mold as described above. To change the dimensions of the sample we have to swap two of the four acrylic side plates for side plates with dimensions $5 \times 35 \times 64$. These dimensions are chosen such that we can fabricate sheets with five holes in the vertical direction. (Fig. 2.6 (a)-(b)) Since we treat the horizontal and vertical boundaries different, as will be described in the following section, we do not have to change the dimensions of the horizontal side plates.

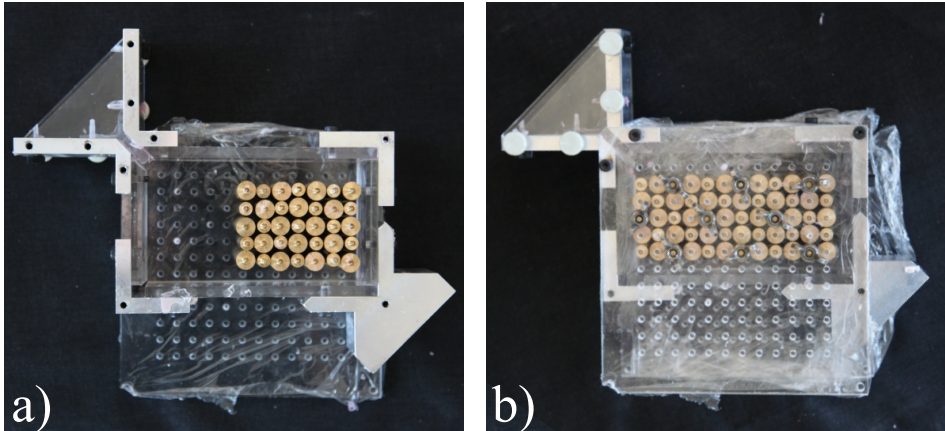


FIGURE 2.5: The assembly of the mold for small samples is very similar to the assembly of the mold for large samples. (a) The mold consists of the same parts as the mold for the large samples, except we have replaced two of the corner plates of dimensions $5 \times 35 \times 120$ mm with two corner plates of dimensions $5 \times 35 \times 64$ mm. These shorter corner plates make the shorter sides of the rectangular mold. Notice that we used cling foil to cover the back plate, see text. Part of the metal cylinders is inserted by piercing them through the cling film. (b) As before, the front plate is mounted onto the mold using $M6$ screws and butterfly nuts.

We start with assembling the corner parts and the acrylic side plates. Next, we mount the back plate. As shown in Fig. 2.6 (b) we can not insert cylinders in all the holes of the front and back plate. This is because the distance between the bottom corner plate and the row of holes right above is too small. To prevent leakage through these empty rows we cover the inner side of the front and back plate with cling film. When inserting the metal cylinders we pierce the pins of the cylinders through the film. We distribute a couple of cylinders with threaded pins, Fig. 2.4 (e) (left cylinder), over the area of the mold. Next we can mount the top plate, which is also covered with cling film. We use the butterfly nuts and the threaded pins to extra tighten the mold to prevent leakage.

2.2.2 Molding

The material used for the biholar metamaterial is a two component silicon elastomer, brand name *Elite Double* from the company Zhermack.¹ The material comes in two bottles, the polymer and the catalyst. The two components of the silicone elastomer have to be mixed in a 1:1 weight ratio. Different types of this product, Elite Double 8, 16, 22 and 32, correspond to different stiffness's and curing times. The curing time varies between 8 minutes and 30 minutes at room temperature. Unless mentioned otherwise, we use Elite Double 8, which has, after curing, a Youngs modulus of $E = 220\text{kPa}$ and an elastic regime of 60% in strain, see Section 2.2.4.

We use a spoon and cup to mix the two components of the silicon elastomer. Due to mixing, air bubbles appear in the fluid and since the fluid is viscous it takes a long time before they disappear. We want to limit the amount of air bubbles in the fluid due to the mixing since they will also show up in the final cured silicone. Hence, we need to remove the air bubbles before the silicone has cured. To do so, we place the fluid for 3 minutes in a vacuum room. This removes most of the air bubbles

We note that the fluid is highly viscous. It takes a long time for the fluid to flow through the narrow channels between the cylinders of the mold. Together with the mixing itself and the time spend in the vacuum chamber this exceeds the work time, the time the polymer is still fluid enough to flow, of the silicon at room temperature, which is ≈ 15 minutes. To increase the work time with the polymer we cool it. Before mixing we place both bottles of the silicon elastomer in a freezer at -18°C to slow down the cross linking time of the polymers. We place the mold in the freezer as well. We place the mold and the material in the freezer for at least two hours. The curing time is increased tremendously by cooling the two components, about 10 times. We slowly pour the mixture into the mold from a distance approximately 20 cm above the mold, resulting in a jet of approximately 3 mm diameter which prevents the trapping of air bubbles in the mold.

Once the mold is filled with the mixture it is positioned in the vacuum room again for 4 minutes at a pressure of to remove air bubbles from the small channels inside the mold.

¹www.zhermack.com – Dutch supplier: Oudheusden Dental BV (www.arseus-lab.nl)

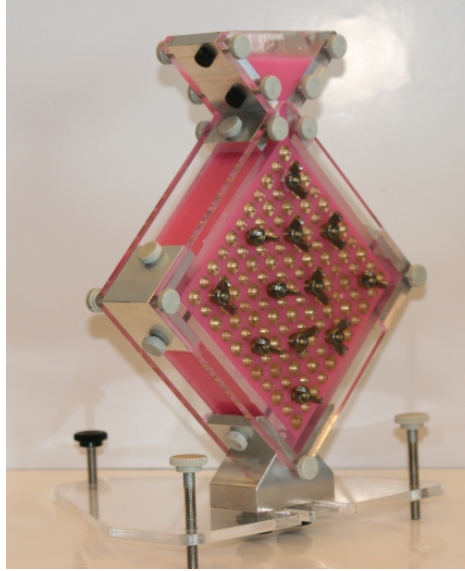


FIGURE 2.6: Assembled mold with silicone elastomer.

Afterward, the mold, with the silicone mixture, is left on a shelf at room temperature for roughly 2 hours. After 2 hours the mixture is sufficiently cured and we can remove the sample from the mold. First the front plate of the mold is removed by unscrewing the butterfly nuts and the five screws fixing the front plate. Then a nipper is used to pull out, one by one, the metal cylinders from the sample. When all metal cylinders are removed the sample can, gently, be separated from the mold.

2.2.3 Sheet Preparation: Cutting, Gluing and Clamping

Once we have taken the sample from the mold, Fig. 2.7 (a), we can prepare the sheet for experiments. We first use scissors to cut the sample to the desired size, Fig. 2.7 (b). The boundaries of the sample are approximately 10 times thicker than the filaments between the holes, Fig. 2.7 (a). Hence, they would dominate the mechanical response of the sample. Therefore we use scissors to remove the lateral sides of the network, Fig. 2.7 (c)-(d). To clamp the sample in our setup, *T*-shaped acrylic structures are glued to the top and bottom of the sheet (Fig. 2.8). These *T*-shaped structure con-

2.2. SAMPLES

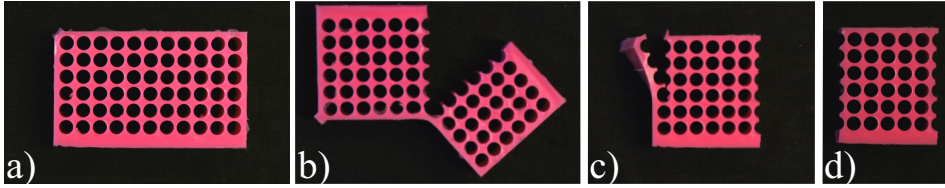


FIGURE 2.7: Giving the sample the desired shape. (a) The sheet as it comes out of the mold for the small samples. (b) We cut the the sample to the right size (c) and remove the lateral boundary. (d) A 5×6 biholar metamaterial.

sists of two parts; (a) a rectangular plate of thickness 5 mm and width 7 cm with two holes in its surface and (b) a rectangular plate of thickness 5 mm and width 5 cm with two long holes all the way through the side of the plate. We first glue plate (a) to the top and bottom boundaries of the network using silicone sealant. To prevent the sealant blocking the holes in the plates we cover these with a small piece of tape. Once the sealant is cured we connect plates (b) to plates (a) using four *M6* screws.

To perform uniaxial compression with lateral confinement experiments, as will be described in Section 2.4, we need to confine the sample in both the x and y -direction. We use clamps to confine the network in the x -direction while compressing the sample in the y -direction by our Instron uniaxial compression device. When we compress the sheet in the y -direction the sides of the sheet describe a concertina motion. We want the clamps to follow this concertina motion. Furthermore it is desired to easily change the amount of clamping between experiments. Therefore a single clamp is designed to consists of four separate parts: two metal pins that are glued to the sheet to follow the concertina motion and two plastic laser cut strips that determine the amount of clamping but are easily changed. We can insert the pins in the plastic strips through laser cut holes at specific positions. The distance between the metal pins, which is set by the distance between the holes in the plastic strips, determines the amount of clamping.

The metal pins have a diameter of 1.2 mm and are cut from electrode wire to lengths of approximately 9 cm. The endpoints of each metal pin are smoothed with a file. Using silicone sealant we glue these metal pins to vertical boundaries of the networks. The metal pins are positioned in the middle of the joint of the removed boundary hole, Fig. 2.8 (a).

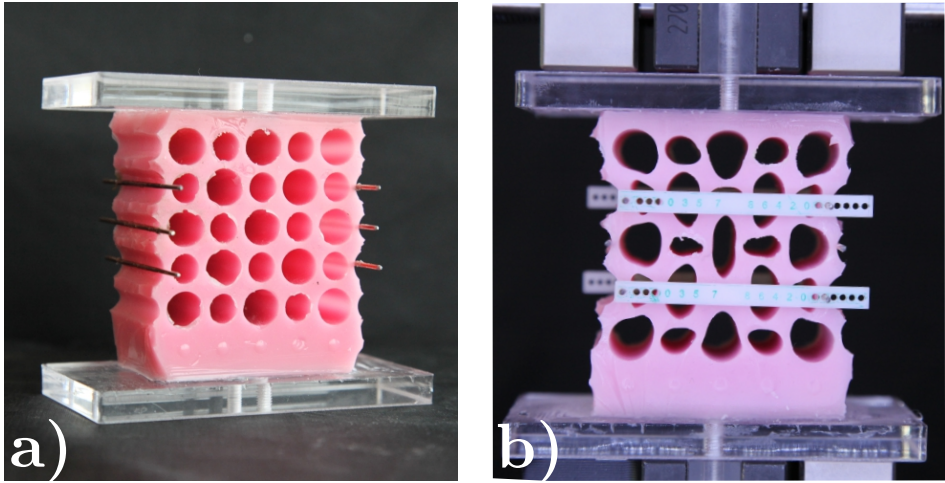


FIGURE 2.8: (a) Biholar network with metal pins glued to the sides of the network. (b) Biholar network with clamps attached to the network by sliding them over the metal pins.

The plastic strips, that slide over the metal pins, are designed on Corel-Draw and fabricated using a laser cutter. The strips, as shown in Fig. 2.8 (b), have dimensions $1 \times 5 \times 55$ mm. The holes have a radii of 1.6 mm to make them slide easily over the metal pins. Since the radius of the holes on the strips are smaller than the desired steps in confinement for a series of experiments, where we typically increase the confinement in steps of 0.5 mm, we fabricate multiple strips with different interholer distances. In this way we can increase the confinement in steps smaller than the radius of the holes on the strips.

The imposed confinement in the x -direction is defined as $\varepsilon_x := 1 - L_c/L$, where L_c is the distance between the metal pins when slided in the holes of the strips (Fig. 2.8) and L is the distance between the metal pins in the unconfined state. This distance L is calculated to be: $(N + 1) \cdot p - D_2$, where N is the number of holes per row, p is the pitch between the center of holes and D_2 is the largest of the two holes.

The accuracy in applied lateral confinement is given by: (1) The accuracy of the positions of the holes on the strips and (2) the precision of positioning and gluing the metal pins to the lateral sides of the sheet, which is done by hand. The accuracy of (1) is set by the resolution of the laser

2.2. SAMPLES

cutter (Universal Versalaser 3.5), already corrected for the width of the focus spot ($250\ \mu\text{m}$), this is within the micrometer range and depends on the stepper motors controlling the movement of the laser beam. The accuracy of (2) is set by the skills of the experimentalist. A misplacement of a metal pin by an amount δ will result in a mistake of approximately $r_2 - \sqrt{r_2^2 - \delta^2}$ in the calculation of L , where r_2 is the radius of biggest hole. With $r_2 = 5$ mm and $\delta = 1$ mm this results in an error of approximately 0.10 mm in the calculation of L_c . With a typical $L = 50$ mm for the smallest systems this, in the end, allows us to control the confining strain of the sheets with a minimum precision of $\frac{0.1}{50} = 0.002$.

2.2.4 Material Properties

Young's Modulus

We now describe the characteristics of the material used to fabricate our biholar metamaterial. Since we deal with a rubber-like material we assume the Poissons ratio of the silicone based rubber to be $\nu = 0.5$ [54]. We find the other constant for linear elasticity, the Young's modulus (E), by performing a uniaxial compression test of a beam with a rest length (l_0) of $45 \cdot 10^{-3}$ m, a depth (d) of $35 \cdot 10^{-3}$ m and varying thicknesses (t) of $t = 3.15, 4.85, 6.05, 8.30, 9.25, 10.20, 10.95, 11.95$ and $12.80 \cdot 10^{-3}$ m, see Fig. 2.9, so we can take the average of the Young's modulus of a set of nine beams.

To fix the beam into the Instron tensile testing apparatus (section 2.3.2) we glue two laser cut T-shaped acrylic plates to the top and bottom of the beam, using silicone sealant, to clamp the beam in the Instron tensile testing apparatus, section 2.3.2.

We compress the beam in the vertical direction by an amount ε_y , where $\varepsilon_y = \frac{l_0 - l}{l_0}$ is the engineering strain, and measure the resulting force ($F(\varepsilon_y)$) for the different thicknesses. Since we are only interested in the material properties for small deformations we make sure we stop compressing the beam before it buckles. Presented in Fig. 2.10 (a) are the force (engineering) strain curves for the varying beam thicknesses. By converting the force to the engineering stress ($\sigma_y = \frac{F}{wd}$) we observe that all different curves collapse onto one master curve.

We use the constitutive equation between the engineering stress (σ_y) and the engineering strain (ε_y) for an incompressible Neo-Hookean beam subjected to a uniaxial load to fit the data and extract the Shear modulus μ [55]:

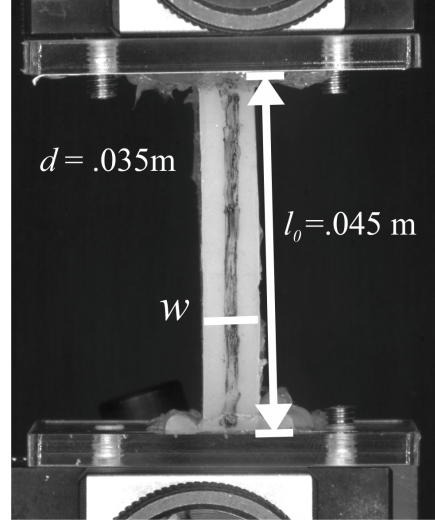


FIGURE 2.9: Uniaxial compression of a beam with parameters l_0 , w and d . Two laser cut T-shaped acrylic plates are glued to the top and bottom of the beam, using silicone sealant, to clamp the beam in the Instron tensile testing apparatus, section 2.3.2.

2.2. SAMPLES

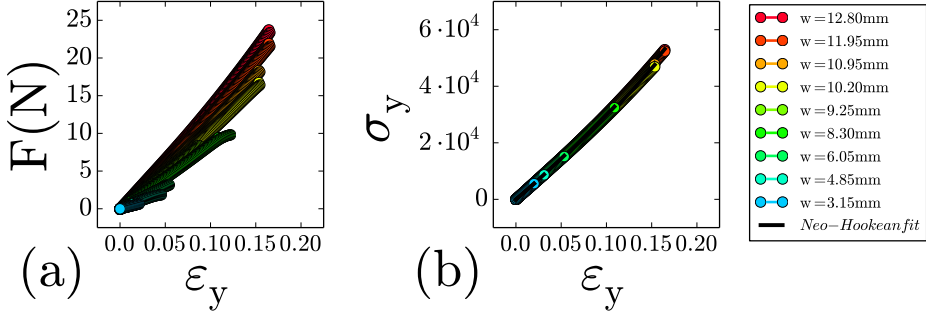


FIGURE 2.10: (a) Force (N) as a function of the engineering strain (ϵ_y) for uniaxial compression for different beam thicknesses (b) By rescaling the force with the area cross section of the beam (dw) we obtain engineering stress (σ_y) as a function of engineering strain (ϵ_y). All curves collapse onto one master curve. In blue the Neo-Hookean fit, Eq. (2.1).

$$\sigma_y = \mu((1 + \epsilon_y) - (1 + \epsilon_y)^{-2}) \quad (2.1)$$

Taking the average of all shear moduli for the different fits corresponding to the different beam thicknesses we find a shear modulus of $\mu = 90.0$ kPa with a standard deviation of $\zeta = 1.6$ kPa. This corresponds to a Youngs modulus of $E = 270$ kPa

Creep and '7-day rule'

At room temperature it takes approximately 20 minutes before the mixture of the two components of the silicon elastomer Elite Double 8 is solid enough such that the material can be removed from the mold. However, the crosslinking still continues for a couple of days, which will effect the stiffness of the material.

Shown in Fig. 2.11 is a measurement of the Youngs Modulus at different times on a dogbone shaped sample with thickness = 34.86 mm, length = 48.5 mm and depth = 10.95 mm. For 9 consecutive days the dogbone was stretched and compressed to ± 4 Newton. The Youngs modulus is obtained by fitting the stress-strain relation for a neo-hookean beam sub-

jected to uniaxial load, Eq. 2.1. The errorbars indicate the standard deviation of the errors of the fit.

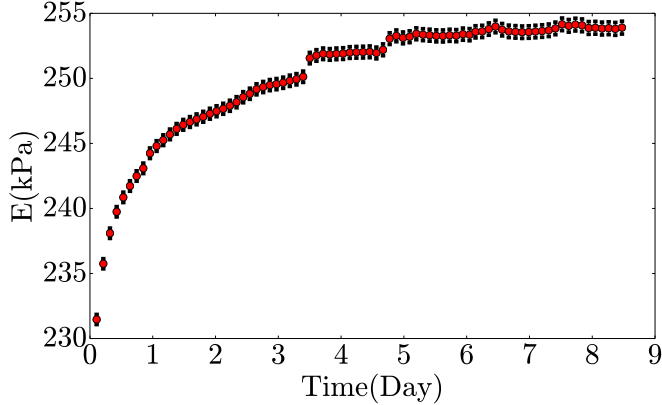


FIGURE 2.11: Measurement of the Youngs Modulus E vs time for 9 consecutive days, performed on a dog bone with dimensions thickness = 34.86 mm , length = 48.5 mm and depth = 10.95 mm made with Elite Double 8. The Youngs Modulus of the material is monotonically increasing for several days until it stabilizes after approximately 5 days.

Observed in Fig. 2.11 is an increase of the Youngs Modulus E of 10% of the material within 5 days. After 5 days the Youngs Modulus stabilizes. Hence, before using a newly made biholar sample for mechanical testing we wait 7 days such that the crosslinking of the two component elastomer has come to an end, the '7 day rule'.

Hysteresis

To understand the effect of the rate of deformations, we have performed a range of experiments with strain rates varying from 10^{-4} to 5 mm/s (Fig. 2.12). The results show that in a broad range of strain rates around 10^{-2} mm/s, spurious hysteresis is minimal. In experiments, a strain rate of 10^{-1} mm/s is chosen to minimize both the spurious hysteresis as well as the time it takes to perform a single experimental run. Moreover, the difference between the up and down sweep peaks when the samples quickly change their configuration, which suggest that viscous effects are responsible for this spurious hysteresis.

2.2. SAMPLES

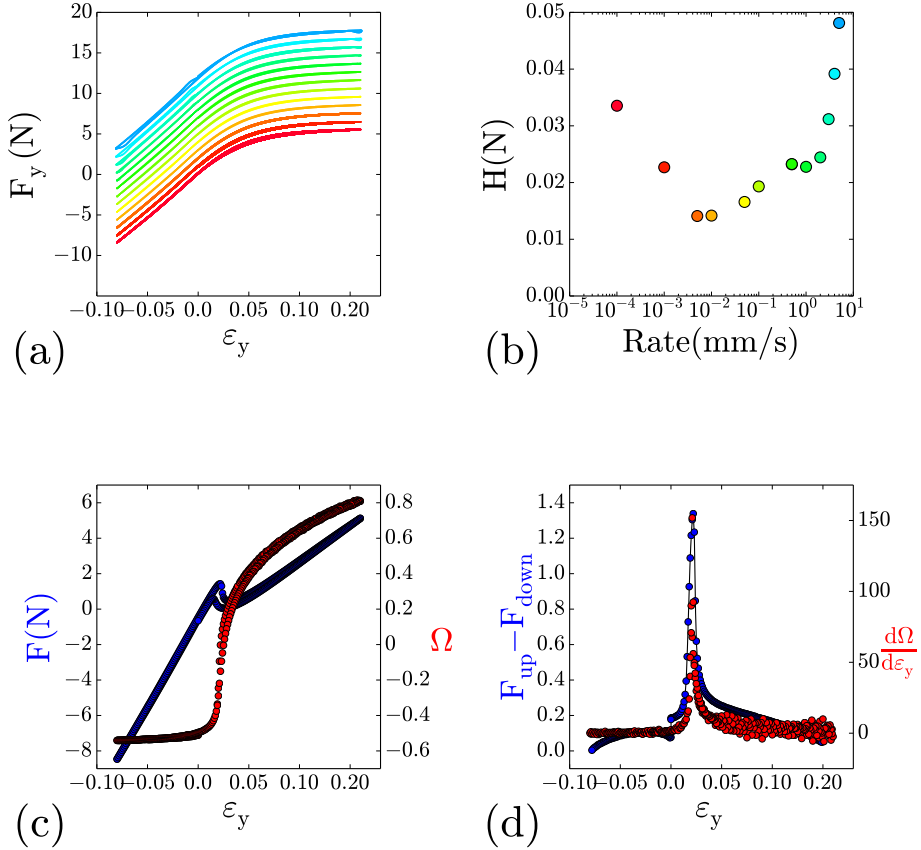


FIGURE 2.12: (a) Force-strain curves for samples with 5×5 holes, dimensionless thickness $t = 0.15$ and biholarity $\chi = 0.2$, for deformation rates varying between 10^{-4} - 5 mm/s (bottom to top). Curves are shown with a vertical offset for clarity. (b) Calculated hysteresis (area of the loop) as a function of deformation rate. (c) In blue the effective stress-strain curve for a samples with 5×5 holes, dimensionless thickness $t = 0.15$, biholarity $\chi = 0.2$ and $\epsilon_x = 0.15$ (regime *ii*), measured at a strain rate of 10^{-1} mm/s. In red the polarization Ω of the central hole as a function of ϵ_y . (d) In blue the difference in force between the up sweep and down sweep as function of ϵ_y , for the blue curve in (c). In red the derivative of the polarization $\frac{d\Omega}{d\epsilon_y}$, for the red curve in (c), as a function of ϵ_y . The good correspondence of the peaks in both data sets strongly suggests that hysteresis is mainly due to weak viscous effects, which are most prominent when the sample quickly changes its configuration.

2.3 Experimental Methods

In the following we start by describing the parameters that we use to characterise the metamaterial and to measure its mechanical response (section 2.3.1). We probe the mechanical response in a uniaxial testing device (Instron type 5965), which controls the compressive strain ε_y and allows us to measure the compressive force F_y (Section 2.3.2). We image the deformations of the material with a CCD camera and track the position and shape of the holes. In section 2.3.3 we describe the experimental protocol. Described in section 2.3.4 are the software tools we use to analyze the force-deformation data and the images.

2.3.1 Parameters

Here we define the parameters that we use to characterize the biholar metamaterial and its mechanical response. **Biholarity.** As shown in Fig. 2.13 we can describe a biholar metamaterial with the parameters D_1 and D_2 , the diameters of the holes and the pitch p . The thickness \tilde{t} of the thinnest part of the filament between two neighboring holes equals $\tilde{t} = p - \frac{D_1 + D_2}{2}$. We define the dimensionless biholarity χ of the sample to be:

$$\chi = \frac{|D_1 - D_2|}{p}. \quad (2.2)$$

When all holes of the sample are of equal size, $\chi = 0$; if $D_1 \neq D_2$, then $\chi > 0$, and χ is always positive. From now on we will identify D_1 with the bigger hole, since this is convenient for the definition of the polarization (see below).

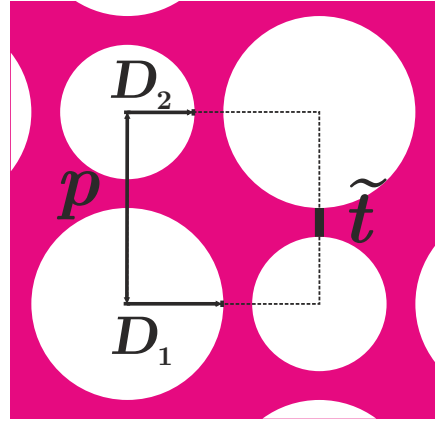


FIGURE 2.13: Overview of the parameters that characterize the sample. D_1 and D_2 are the two radii of the holes. The distance between the center of these holes is given by the pitch p . The thinnest part of the filament between two neighboring holes is called the thickness \tilde{t} .

Dimensionless thickness. Shown in Fig. 2.13 is the thickness \tilde{t} , the thinnest part of the filament between two neighboring holes. The dimensionless

2.3. EXPERIMENTAL METHODS

thickness is obtained by dividing the thickness t by the pitch p :

$$t = \frac{\tilde{t}}{p} = 1 - \frac{(D_1 + D_2)}{2p} \quad (2.3)$$

Polarization. During compression of the confined biholar metamaterial we expect the hole pattern to change to a pattern of small and big ellipses (section 1). We will track this pattern change by focusing on the "polarization (Ω)" of the holes. We define the polarization of the holes as follows:

$$\Omega = \pm(1 - p_2/p_1) \cos 2\phi, \quad (2.4)$$

where p_1 is the major axis of the ellipse, p_2 the minor axis of the ellipse and ϕ the angle between the major axis and x -axis. Ideally, for regular patterns, ϕ is either 0 or $\pi/2$, but for realistic patterns ϕ can have different values. Note that the major axis of the large ellipses is in the x -direction for y -polarized systems (Fig. 2.2(c)). As the values of ϕ of the small and big holes are different, we define the sign of Ω such that Ω is positive for y -polarization and negative for x -polarization.

Strain. We apply two different strains to our sample. The confining strain ε_x , applied by the clamps, and the compressive strain ε_y , applied by the Instron testing machine. We define the confining strain in the x -direction as:

$$\varepsilon_x = 1 - L_c/L, \quad (2.5)$$

where L_c is the distance between the metal pins that are glued to the lateral sides, of the sample (section 2.2.3) in the *confined* state and L is the distance between the metal pins in the *unconstrained* state.

As can be seen from Fig. 2.14, for samples with an uneven amount of columns the distance L will differ between the even

and uneven rows. Unless mentioned otherwise, we will always use samples with an uneven amount of columns, with a large hole in the center. Also, for now, we only clamp rows that end in small holes, such that

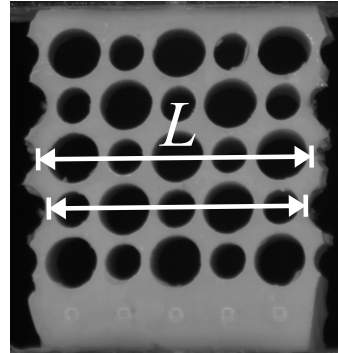


FIGURE 2.14: The distance between the metal pins L will differ between the even and uneven rows for a sample with an uneven amount of columns.

$L = (N_r + 1)p - D_1$. Since we only clamp every second row, the *averaged* horizontal strain is smaller than the control parameter ε_x .

Moreover, since all the deformations occur in the 'holey' part of the sample and not at the thick top and bottom boundaries, we define the compressive strain in the y -direction as:

$$\varepsilon_y = u_y / N_c p, \quad (2.6)$$

where u_y is the imposed displacement/deformation applied by the Instron testing machine with respect to the height ($N_c p$) of the sample in the unconstrained state, N_c is the number of holes per column and p the pitch. Note that we defined both strains to be positive when we compress the sample and negative when we stretch.

2.3.2 Experimental setup

Uniaxial Testing

We use a dual column Instron 5965 uniaxial testing device to compress the sample in the vertical direction and measure the resulting force (Fig. 2.15). The sample is clamped in the Instron testing machine between the ground plate and a moving horizontal bar, using two metal clamps from Instron. The Instron moves the horizontal cross bar in the vertical direction with a resolution of $4 \mu\text{m}$. The resulting force F is measured with a 100 N load cell, attached to the horizontal moving bar. The resolution of the load cells manufactured by Instron are given by $\pm 0.5\%$ of reading down to $1/1000$ of load cell capacity. Hence, for the 100 N load cell we can accurately measure forces as low as 0.5 mN, while the typical forces we measure are of order 1N.

Both the Instron testing device and the load cell are computer controlled. We use the BlueHill 2 software to control the movement of the vertical bar and measure the response of the load cell. In the workspace of the BlueHill 2 software we can design a testing protocol. The testing protocol will depend on the experiments performed and will be described in more detail below. The data obtained from the load cell and the movement of the horizontal bar is saved as in a '.csv' file.

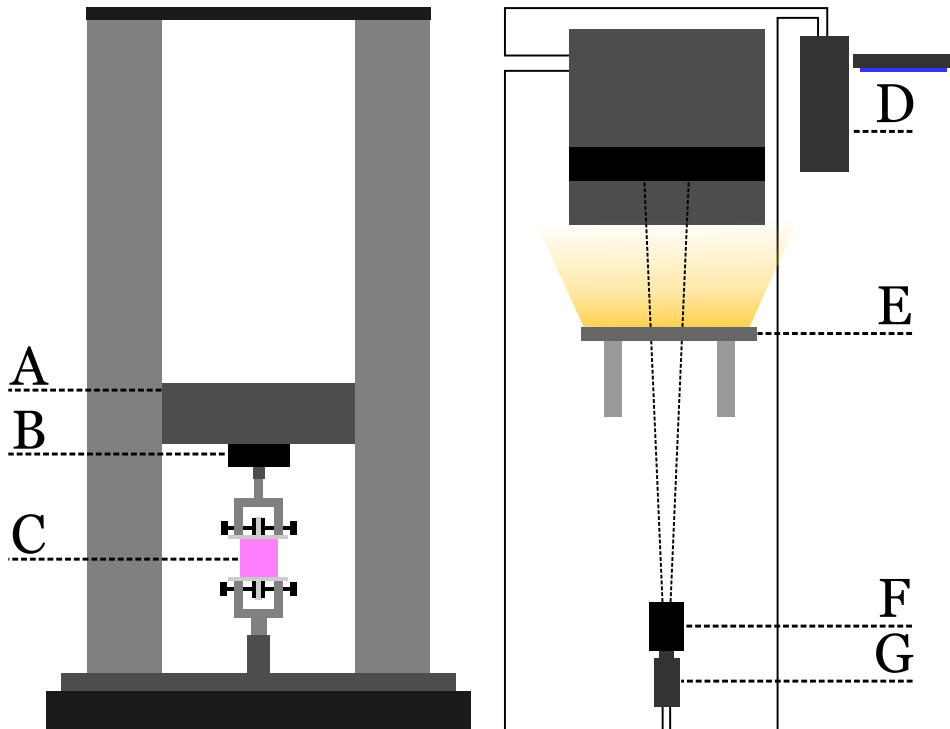


FIGURE 2.15: Overview of the setup. (A) Horizontal cross bar. (B) Loadcell. (C) Sample. (D) Computer. (E) LED-light panel. (F) Lens. (G) Camera.

Imaging

A camera is installed to acquire images of the deformation of our samples and track the position and shape of the holes. This allows us to determine the polarization of the holes. We use a Basler acA2040-25gm/gc CMOS camera (2046×2046 pixels, pixel size $5.5 \times 5.5 \mu\text{m}$). The camera is placed approximately 90 cm away from the sample to minimize parallaxing and only focus on the front plane of the sheet, resulting in a spatial resolution of 0.03 mm.

The camera is connected to the same computer as the Instron testing device and is controlled using LabView. The image acquisition is synchronized with the data acquisition of the Instron. To synchronize the data acquisition with the image acquisition we use the SYNC output of the Instron testing device to trigger the camera. The output of the SYNC connec-

tion is a pulse, with pulse height of 5 V and a pulse width of $4\mu\text{s}$, running simultaneously with the data acquisition of the load cell. This pulse is only available in BlueHill 2 or older versions of the BlueHill software. Using the SYNC pulse of the Instron it is possible to acquire an image for every data point measured with the Instron testing machine.

We illuminate the front to the sample with DCLED lights. In order to obtain pictures of high quality and not over- or underexposed to light, we need to choose an exposure time between 150 ms and 750 ms. Hence, the period of data acquisition of the Instron, that controls the SYNC pulse, has to exceed this, which is not a problem as our experiments are done slowly. The data obtained from the camera is saved in a separate folder as 'PNG' files.

2.3.3 Experimental Protocol

We start the experiment by placing the sample in the Instron. We first clamp the acrylic T-shaped top part in the Instron tension machine and zero the force, using the 'Balance load'-button. We then lower the crossbar with the sample using the manual control panel of the Instron until the top of the T-shaped bottom hits the clamp and the force is slightly increased, in the order of 0.01 N. Now we also fix the bottom part of the sample and set the force and displacement to zero ('Balance load'-button and 'Reset Gauge'-button).

Next we adjust the camera. The DCLED lights are turned on, and start the LabView NI-DAQmx Measurement & Automation Explorer software to control the camera and capture the images. We untick the triggermode box of the software and play 'capture images continuously' so we can observe the view of the camera. We adjust the position of the camera such that the sheet is in the center of the image. Now we use the lens to zoom in such that the entire area of the image on the screen is filled with the image of the sheet. If needed, we adjust the position of the camera again such that the sample is in the center of the image.

Next, we focus the camera on the front plane of the sheet. This is done manually with the Tamron AF aspherical XR lens attached to the camera. We then stop capturing images continuously to be able to choose the exposure time of the camera.

As mentioned in section 2.3.2, the data acquisition of the camera is synchronized with the data acquisition of the Instron. The maximum rate of

2.3. EXPERIMENTAL METHODS

data acquisition of the Instron is 2.5 kHz, while that of the camera is 25 Hz. Hence, the data acquisition rate is limited by the data acquisition rate of the camera. The data acquisition is even more limited by the exposure time of the camera, we demand high quality bright images for image analysis. Consequently, we first need to set the exposure time of the camera. We choose an exposure time of 0.05 seconds, this gives, in combination with the DCLED light panels, images of good exposure and a lot of contrast. We also need to reserve some time for the software to acquire and save the images. Hence, the time interval between two successive data points has to be longer than the image acquisition and saving time plus the exposure time of 0.05 seconds. We set this time interval to be 0.5 seconds, ergo we obtain two data points and two synchronized images per second.

Next, we start the Bluehill 2 software. We designed a test that allows us to compress and decompress the sheet by an amount u_y , with a rate of 0.1 mm per second and make sure that we save the data in a .csv file, where the columns are time, displacement and force. The compression rate of 0.1 mm per second is chosen such that if we compress and decompress the sample by 10 mm with an acquisition rate of 2 Hz we obtain 400 pictures or data points. This is high enough resolution to characterize the force and polarization curves. Now, in parallel, we start our self written lab-view program that captures the pictures taken with the camera triggered by the SYNC pulse.

We attach the clamps such that they confine the sheet by an amount u_x . Next, start the LabView program and immediately after we start the designed Bluehill program, such that we can collect the images and force data. We have written the Labview code such that if the software does not receive a trigger pulse for 5 seconds it will stop.

The data from the Instron is save in a folder named 'Data' and the images are save in a folder named 'Pictures'. The folders 'Data' and 'Pictures' are in a folder named 'ux***mm', where on the '***' we write the amount of clamping. Furthermore, the folder named 'ux***mm' is placed in a folder named 'D##D##_..X..', where on the '##' we write the diameters of the holes of the sample and on the '..' the amount of holes on the rows and columns of the sample.

2.3.4 Image analysis

As mentioned above we acquire two different sets of data, the force-displacement data from the Instron and the images from the camera. Here we describe the steps needed to retrieve the polarization of the holes from the pictures.

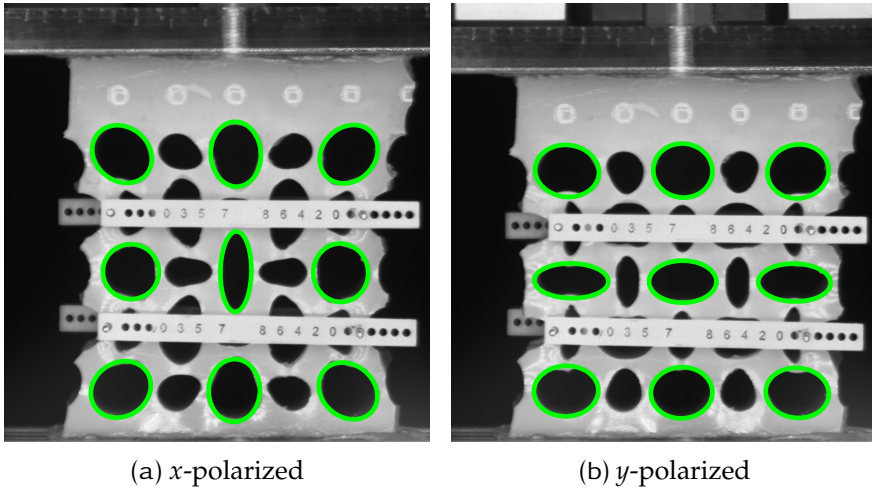


FIGURE 2.16: The fitted ellipses, that are found using the protocol described in this section, are drawn on top of the images of the bi-holar sheet ($\chi = 0.3$ and $t = 0.15$ and $\varepsilon_x = 0.127$). (a) The fits drawn on top of the sample for the sample in the x -polarized state. (b) The fits for the sample in the y -polarized state.

The goal for the image analysis is to get the polarization (section 2.3.1) of the holes and be able to track the polarization during compression. To do so we use the Python package OpenCV2.

We first threshold (`cv2.threshold(arguments)`) the image, so we have a black and white image instead of an image in greyscale. Next, we blur (`cv2.blur(arguments)`) the image and use the function

`cv2.findContours(arguments)` to find all the contours in the image. We use the function `cv2.fitEllipse2(arguments)` to do the actual fitting of the ellipses. This function fits ellipses to the contours of the image and returns x and y -values of the center of the ellipse, the length of major axis p_1 , length of the minor axis p_2 and the angle ϕ of the major axis with respect to the x -axis. From these parameters we can calculate the polarization:

$\Omega := \pm(1 - p_2/p_1) \cos 2\phi$, section 2.3.1.

As a check we draw the ellipses on top of the greyscale image using `cv2.ellipse(arguments)`, see Fig. 2.16. Using a tracking algorithm we follow the ellipses during compression so we finally obtain $\Omega(\varepsilon_y)$ for every fitted ellipse.

2.4 Programmable Mechanical Response

In the following we will characterize the mechanical behavior of the bi-holar sample as function of lateral confinement. To do so, we will measure the force $F_y(\varepsilon_y)$ as a function of the deformation in the y -direction (ε_y) while applying a confining strain, ε_x , in the x -direction.

The parameter space is very large, as we can vary χ and t (see Chapter 5). For now we will focus on a single bi-holar sheet with $\chi = 0.3$, $t = 0.15$ and rigid clamps. As we will see in Chapter 5, inhomogeneities play an important role for large systems, so to probe the mechanics of asymptotically large *homogeneous* materials, we start our exploration with the smallest experimentally feasible building block, a 5×5 bi-holar sheet.

In Fig. 2.17 we present the force $F_y(\varepsilon_y)$ and polarization $\Omega(\varepsilon_y)$ of the large center hole for a range of values of ε_x . The curves are shown with an offset for clarity. We can distinguish four qualitatively different types of mechanical response: a monotonic regime (*i*); a non-monotonic regime which features a range of ε_y with negative incremental stiffness (*ii*), a hysteretic regime (*iii*); and a second monotonic regime (*iv*).

(i : MONOTONIC REGIME) For $\varepsilon_x \lesssim 0.09$, the force increases monotonically with ε_y (Fig. 2.17(a)). The polarization of the large central hole smoothly grows from its initial non-positive value (full part of the curves) to positive values (dashed part of the curves) with ε_y (Fig. 2.17 (b)).

The *initial* value of the polarization becomes more negative with increasing the lateral confinement (the thin pink line indicates $\Omega = 0$ for each curve). This can be understood, as for $\varepsilon_x = 0.00$, the holes of the sample are circular at $\varepsilon_y = 0$ (p_1 and p_2 in Eq. 2.4 are equal) hence, $\Omega = 0.0$. Increasing ε_x makes the pattern more and more x -polarized resulting in a decrease of Ω at $\varepsilon_y = 0$ (since $p_1 > p_2$ in Eq. 2.4).

Now, compressing the initially x -polarized pattern transforms the patterns

smoothly, in this regime, to a y -polarized pattern, crossing the line $\Omega = 0$ for increasing values of ε_y . All force curves in this regime show strain weakening. This effect is increasing when the confining strain ε_x is increased. The strain weakening in the force curves can be associated with the change of sign in the polarization.

(ii NON-MONOTONIC REGIME) Now increasing the lateral confinement, $0.10 \lesssim \varepsilon_x \lesssim 0.13$, $F_y(\varepsilon_y)$ becomes non-monotonic — here the material has negative incremental uniaxial compressibility around $\varepsilon_y = 0.04$. The polarization remains monotonically increasing with ε_y but gets focused in this ‘negative slope’ region.

First the force increases, then, for $0.04 < \varepsilon_y < 0.06$, less force is needed to compress the sample further and finally the forces increases again. The difference between the local maximum and local minimum of $F_y(\varepsilon_y)$ increases with increasing lateral confinement. Note that the small hysteresis in this regime between compression and decompression is due to weak visco-elastic and creep effect of the material used to fabricate these samples (see section 2.2.4).

(iii HYSTERETIC REGIME) Next, for $0.14 \lesssim \varepsilon_x \lesssim 0.16$, $F_y(\varepsilon_y)$ exhibits a hysteretic transition, i.e. it follows a different path for compression and decompression. In the polarization we observe a corresponding hysteretic switch from x to y polarization. Note that in this case, the polarization is non-monotonic and initially decreases. Hence, y -compression makes the center hole initially more x -polarized, before it causes the material switch to a y -polarized state. The force first increases monotonously, before it jumps to a lower branch. The location of the jump shifts towards higher values of ε_y for increasing lateral confinement. When decompressing, the force initially follows the identical path except, at the location of the jump in the compression path, it smoothly traces out a different path, before the force starts to increase and rejoins the compression curve at $\varepsilon_y \approx 0.04$. The location where the curves reunite appears to be independent of ε_x . The area between both curves, the hysteresis, increases with increasing lateral confinement.

The location of the switching of the polarization is different for compression and decompression. For compression, it shifts towards higher values of ε_y for increasing ε_x . For decompression it appears to be independent of ε_x . Again, the hysteresis increases with increasing lateral confinement.

(*iv* **2nd MONOTONIC REGIME**) Finally, increasing the lateral confinement even more, $\varepsilon_x \gtrsim 0.17$, we observe a second monotonic force curve, with strain weakening. However in contrast to regime *i*, the material does no longer switch from *x*-polarized to *y*-polarized but becomes increasingly strongly *x*-polarized. We note that in this case, additional experiments reveal that initial compression in the *y* direction followed by *x*-confinement brings the material to a strongly *y* polarized state. Hence, for strong biaxial confinement there are two stable states, that are so different that uniaxial compression is not sufficient to make them switch.

We have explored this scenario for a number of different biholar sheets, and find the same four types of responses, provided that $0 < \chi \lesssim 0.06$ and $t \lesssim 0.2$, see chapter 4. Moreover, as we will discuss below, such behavior is also found in larger systems. Hence, we conclude that confined biholar sheets can be tuned to exhibit *four* qualitatively different types of mechanical behavior.

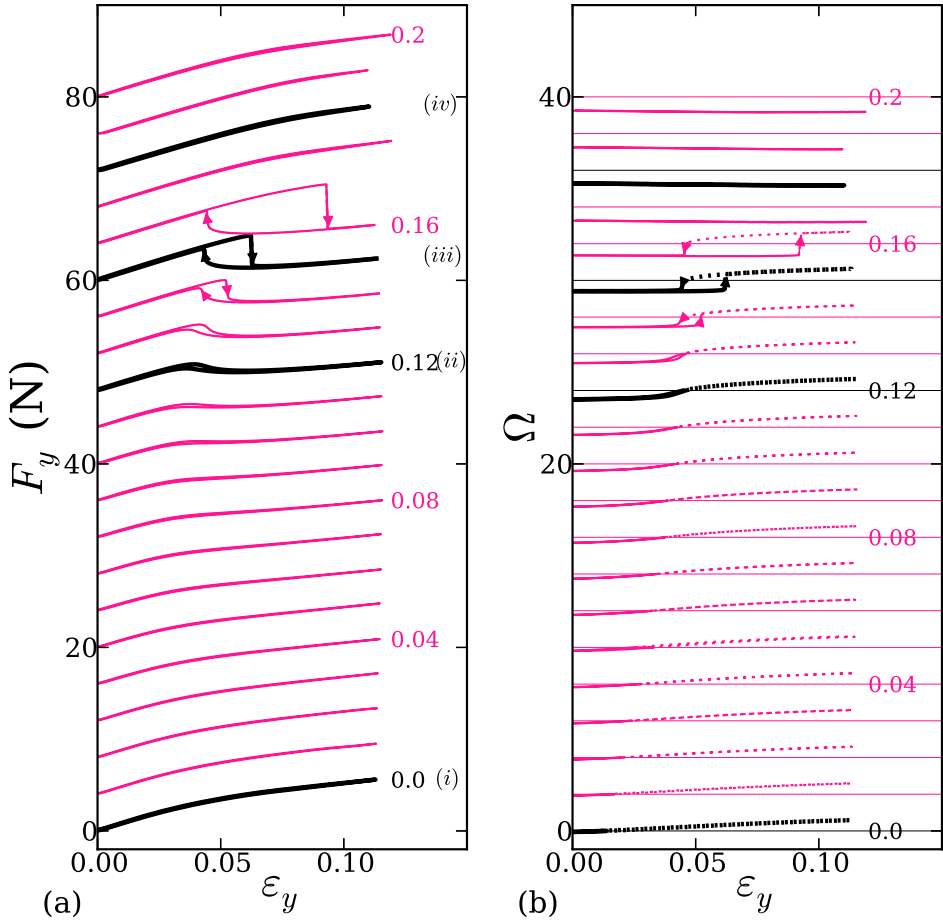


FIGURE 2.17: (color online) Mechanical response of a 5×5 sheet with $D_1 = 10$ mm, $D_2 = 7$ mm ($\chi = 0.3, t = 0.15$) for increasing confinement ε_x [56]. Curves are offset for clarity. (a) The force curves $F_y(\varepsilon_y)$ show monotonic, non-monotonic and hysteretic behavior. The curves labeled (i)-(iv) correspond to four qualitatively different behaviors. (b) Polarization of the large center hole, where full (dashed) curves indicate negative (positive) values. For movies of case (i)-(iv), see supplementary material of [57].

2.5 Numerics

To probe whether these phenomena are robust, we have performed 2D plane strain finite element simulations (Abaqus) of a Neo-Hookean material on a 2×2 unit cell using periodic boundary conditions (Fig. 2.20). To probe numerically the various equilibrium branches (discussed in detail in Chapter 3), hysteresis and bistability, we use two different protocols — in protocol A we first apply a confinement ε_x and then a compression ε_y (Fig. 2.18), whereas in protocol B we first apply a large compression in the y -direction, then a confinement ε_x and finally decompress in the y -direction until we reach $\varepsilon_y = 0$ (Fig. 2.19).

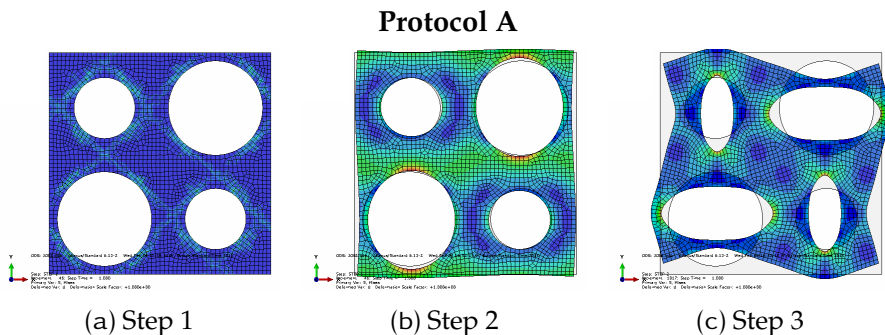


FIGURE 2.18: (a) The unstressed unit cell, step 1. (b) We first compress the unit cell in the horizontal direction, where the top and bottom boundary are stress free, step 2. (c) We keep the lateral boundaries fixed and we compress the unit cell in the vertical direction, step 3.

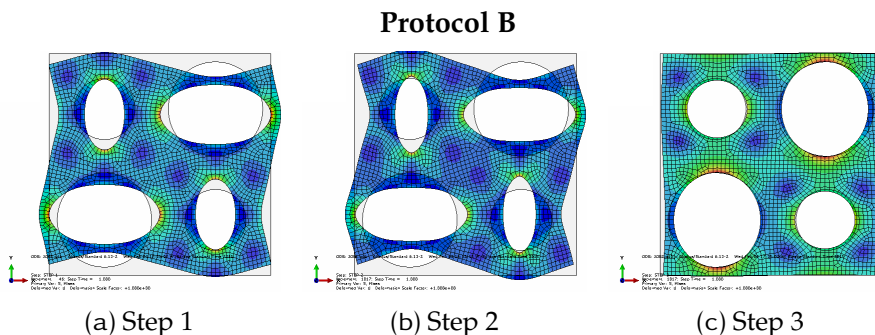


FIGURE 2.19: (a) First, the unit cell is maximally vertical compressed. (b) Horizontal confinement is applied. (c) The unit cell is decompressed in the vertical direction to $\varepsilon_y = 0$

As shown in Fig. 2.20, these simulations exhibit the four types of behavior (i)-(iv) observed in experiments. Moreover, these simulations reveal that in case (iv), the x and y -polarized branches become disconnected, consistent with our experimental data. The correspondence between experiments and simulations on systems with periodic boundaries show that our findings represent robust, bulk-type behavior, and suggest that biholar metamaterials of arbitrary size remain functional.

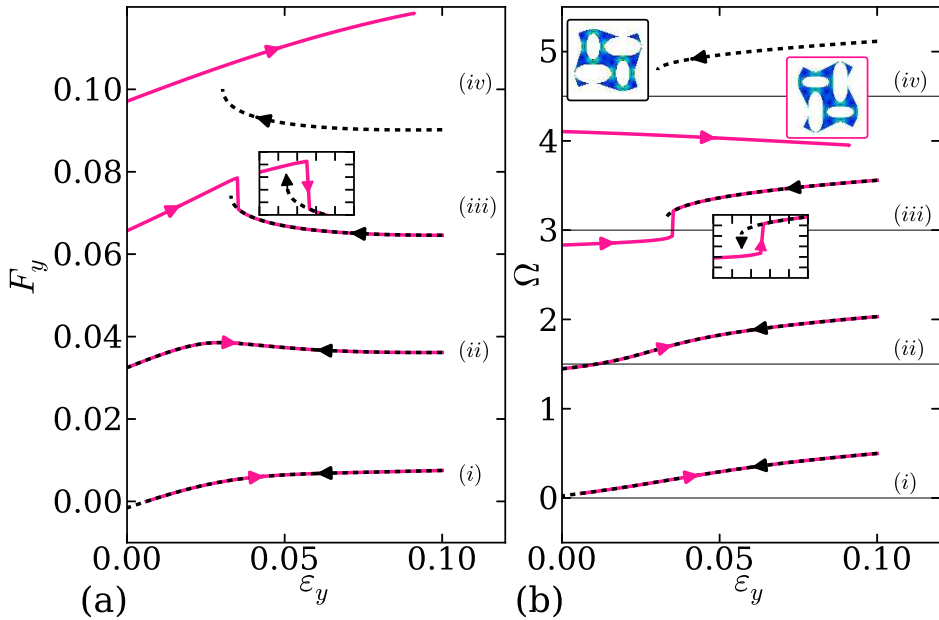


FIGURE 2.20: (color online) Finite element simulations on a unit cell with periodic boundary conditions and $\chi = 0.3, t = 0.15$. (a) Force F_y and (b) polarization Ω , for (i) $\epsilon_x = -1.0 \times 10^{-2}$, (ii) $\epsilon_x = 2.8 \times 10^{-2}$, (iii) $\epsilon_x = 3.4 \times 10^{-2}$, (iv) $\epsilon_x = 7.5 \times 10^{-2}$. Full (dashed) curves correspond to protocol A (B). For a movie of case (iii), see supplementary material of [57]

2.6 Soft Mechanism

To qualitatively understand the mechanics of confined biholar sheets, we note that when $t \rightarrow 0$, the material's low energy deformations are equivalent to that of a mechanism of rigid rectangles coupled by hinges located at the necks of the "beams" (Fig. 2.21). The state of this mechanism is described by a single degree of freedom, θ , which determines the internal dimensions x_i and y_i . To model the storing of elastic energy, we couple this mechanism to outside walls at spacing x_o and y_o via a set of linear springs with zero rest length and spring constant $1/2$ (Fig. 2.21c).

As Fig. 2.21a-b shows, such simple model qualitatively captures the full experimentally and numerically observed scenario, when we identify the clamping ε_x with $1 - x_o$ and compression ε_y with $1 - y_o$ (Fig. 2.21a-b).

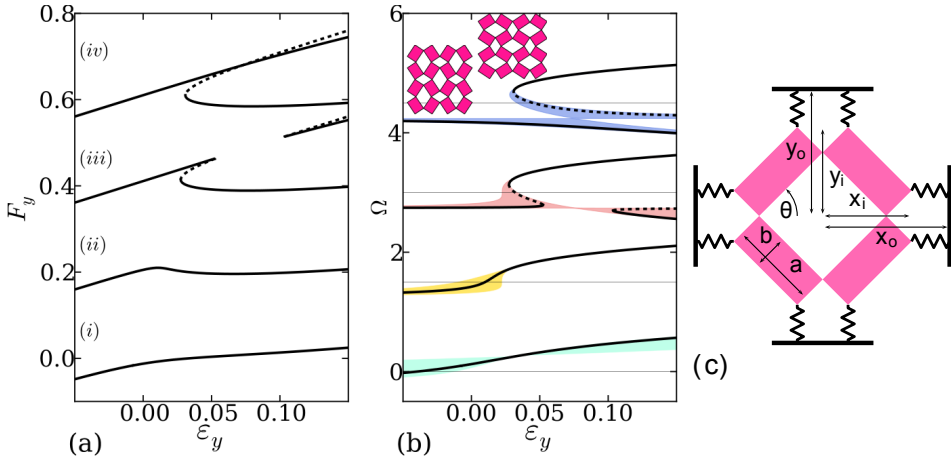


FIGURE 2.21: (a-b) The force and polarization in our mechanical model for $\chi = 0.3$ ($a \approx 0.81, b \approx 0.6$) exhibit behaviors (i)-(iv) — here full (dashed) curves correspond to stable (unstable) equilibria, and the insets show a y and x -polarized state. The colored regions in (b) are obtained by sweeping x_o through the ranges (i)-(iv) and tracing out the corresponding polarization curves. (c) Soft mechanism, with $\chi = 2(a - b)/(a + b)$, and where the undeformed configuration corresponds to $\theta = \pi/4$, so that $a + b = \sqrt{2}$. For movies, see supplementary material of [57].

2.7 Conclusion

We have introduced a new class of programmable mechanical metamaterials whose functionality rests on two pillars: First, confinement allows to store and release elastic energy, crucial for complex mechanics. Second, a broken symmetry leads to competition and coupling between a secondary confinement and a primary strain.

By varying the secondary confining strain we observe 4 qualitatively different mechanical responses, regimes (i)-(iv). This is a robust phenomenon, is highly reproducible and is seen in experiments, numerics and a simple model. From the numerics we conclude that the phenomenon is a bulk type behavior. Hence, the behavior is scalable and systems of arbitrary size remain functional.

The correspondence between the simple soft mechanism model and the numerics and experiments demonstrates that we have captured and understood the underlying physics. We can understand the origin of the 4 different regimes by a simple geometric picture. We expect to see even more resemblances, between on one hand the model and on the other hand the numerics and experiments, qualitatively and quantitatively, if we expand the model with, for instance, torsional springs [58].

Finally, our work leads to several open questions. First, what is the role of the geometry, the dimensionless parameters χ and t , on the mechanics of these biholar meta materials (Chapter 4)? What is the effect of the position of the clamps (Chapter 5)? For large, inhomogenous and multi-stable systems, how many distinct states can be reached when more complex parameter sweeps are allowed (Chapter 5)? Can we rationally design mechanical metamaterials with confinement controlled response? Can we connect the mechanics of biholar sheets to the well-studied holey sheets with equal hole sizes, for which the mechanical response is not fully understood [42, 44–47, 50, 51]?

2.7. CONCLUSION
